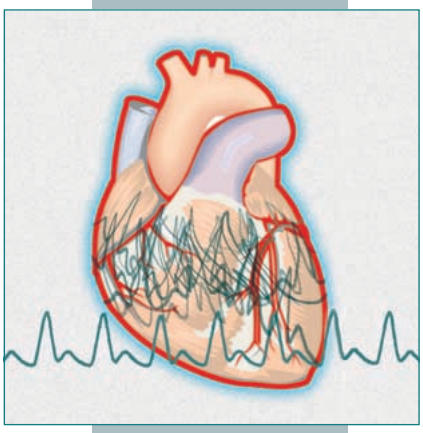

©COREL

Dimensional Analysis of HRV in Hypertrophic Cardiomyopathy Patients

Can the Correlation Dimension Discriminate Patients with Low Risk of Sudden Cardiac Death from High-Risk Patients?

R. Carvajal[1,2], J.J. Zebrowski[3], M. Vallverdú[1], R. Baranowski[4], L. Chojnowska[4], W. Poplawska[4], P. Caminal[1]

[1]ESAII Department, Biomedical Engineering Research Centre, Technical University of Catalonia, Spain
[2]Faculty of Computer Sciences, Autonomous University of Sinaloa, México
[3]Institute of Physics, Warsaw University of Technology, Poland
[4]National Institute of Cardiology, Poland

Hypertrophic cardiomyopathy (HCM) is an excessive thickening of the heart muscle in the absence of an apparent cause. This condition excludes individuals with high blood pressure or prolonged athletic training. It is characterized by left and/or right ventricular hypertrophy, which is usually asymmetric. It is a familial disease with autosomal dominant inheritance caused by mutations in the sarcomeric contractile protein gene [1]. The electrocardiogram (ECG) of those patients who have this pathology shows an abnormal electric signal due to the thickening of the heart and the loss of the normal alignment of heart muscle cells. Some HCM patients can develop arrhythmias (ventricular tachycardia and atrial fibrillation), endocarditis, heart block, and also sudden cardiac death (SCD). In HCM patients there is an increased risk of premature death, which can occur with little or no warning. SCD can strike at any age [2]. However, stratification for sudden cardiac death on patients with HCM is highly difficult [3].

There have been some attempts to identify HCM patients at high risk of SCD using cardiac signals, analyzing the QT interval in the time domain [4], and the time-frequency representation of heart-rate variability (HRV) [5]. The analysis of HRV has been relevant in the study of several cardiovascular phenomena. A great advantage of HRV analysis is that it is a noninvasive technique [6]. A representative discrete-beat series (RR series) of HRV is obtained from the ECG, and it is defined as the time between two consecutive R-peaks.

In this article, the HRV signals of 16 HCM patients are analyzed. Eight of them died or had a history of aborted sudden cardiac death, forming the high-risk group (SCDHCM). The other eight patients form the low-risk group (HCM). Stationarity analysis is applied in order to avoid nonstationarities and to reject those data from further analysis. The surrogate data method is used to test nonlinear determinism on the RR series. Correlation dimension is calculated for all of the signals. An exponential fit to obtain the D_c is introduced, and a new index, $D_c k$, derived from the proposed methodology is presented. This new phenomenological index will have the ability to stratify HCM patients with low and high risk of sudden cardiac death.

Overview

The natural pacemaker of the heart is the sinuatrial node, which is controlled by the autonomic nervous system. This system has two branches: the sympathetic system and the vagal system. The former has an activation effect, while the latter has an inhibitory activity. Both constitute a complex regulation system resulting in heart rhythm regulation. HRV may reflect the sympathetic-vagal interactions occurring during the control of cardiovascular functions. In general, low variability in the heart rhythm is associated with bad prognosis and risk of cardiac dysfunction [7].

Several time-domain measures of HRV have been applied for clinical and limited research purposes. These measures provide only an overall HRV measure. Spectral analysis of the RR time series is a better representation of the different physiological sources of the heart beat generation. However, the traditional techniques of data analysis in time and frequency domains are often not sufficient to characterize the complex dynam-

 0739-5175/02/$17.00©2002IEEE

Correlation Dimension

From a defined data vector $(y_i, i = 1, \ldots, N)$, where N is the number of samples, the points in an m-dimensional phase space (embedding dimension) are constructed, according to the Takens theorem [29], obtaining:

$$\vec{x}_t \equiv (y_t, y_{t+\tau}, y_{t+2\tau}, \ldots, y_{t+(m-1)\tau}),$$
$$t = 1, \ldots N - (m-1)\tau \quad (5)$$

where τ is the time-delay or lag, expressed as a number of beats.

Grassberger and Procaccia [30] showed that D_c can be obtained from:

$$D_c = \lim_{r \to 0} \left[\frac{\log_2(C_m(r))}{\log_2(r)} \right] \quad (6)$$

where $C_m(r)$ is the correlation integral, which measures the number of points x_j that are correlated with each other in a sphere of radius r around the points x_i. This algorithm is also known as the sphere counting method. Thus, in the phase space, the correlation integral $C_m(r)$ is defined as:

$$C_m(r) = \lim_{N \to \infty} \frac{1}{[N-(m-1)\tau][N-(m-1)\tau-1]} \times \sum_{i=1}^{N-(m-1)\tau} \sum_{j=i+1}^{N-(m-1)\tau} \Theta\,(r - ||\vec{x}_i - \vec{x}_j||) \quad (7)$$

where $\Theta(z)$ is the Heaviside function:

$$\Theta(z) = 0 \quad \text{if } z \le 0$$
$$\Theta(z) = 1 \quad \text{if } z > 0$$

and $||x_i - x_j||$ is the distance between a pair of points in the attractor. In the present work, this distance is computed as the Euclidean norm; i.e.,

$$||\vec{x}_i - \vec{x}_j|| = \sqrt{\sum_{k=1}^{m} (x_{i,k} - x_{j,k})^2} \quad (8)$$

where m is the dimensionality of the phase space corresponding to the embedding dimension.

When $\log_2(C_m(r))$ is plotted versus $\log_2(r)$, the slope of the resulting straight line, determined by linear regression at low r (6), yields the correlation dimension D_c. Several $C_m(r)$ are computed for increasing values of the embedding dimensions m, and the slopes are determined from a *scaling region* of the log-log plot, obtaining a sequence of $d(m)$. As m is increased, $d(m)$ tends to a constant value of saturation, which is the value of D_c [31].

In practice, it has been shown that it is sufficient to take randomly only 10% of the points as reference points (N_{ref}) to calculate the correlation integral [32]:

$$C_m(r) = \frac{1}{N_{ref}[N-(m-1)\tau-1]} \times \sum_{i=1}^{N_{ref}} \sum_{j=i+1}^{N-(m-1)\tau} \Theta\left(r - \left\|\vec{x}_i - \vec{x}_j\right\|\right). \quad (9)$$

For each reference point, the distance to all other points in the attractor is calculated except for those points that are correlated with the reference point (i.e., the nearest neighbors in time), avoiding autocorrelation effects. The number of neglected points corresponds to three to five points around the reference point. This procedure is known as Theiler correction [33].

Parameters Related with D_c Calculation

Using the criterion that the amount of data points (N) must be at least $10^{Dc/2}$ [31], and in accordance with preliminary results [34], it was determined that about 10,000 beats are needed for the computation of D_c.

Two criteria were taken into account to select the lag or time delay (τ). In the first one, the system was considered as a discrete time system (map) applying then τ = 1 [35]. In the second one, the system was considered to be a continuous time system and the τ was selected as the first relative minimum of the autocovariance function (ACF) [36] (Figure 1).

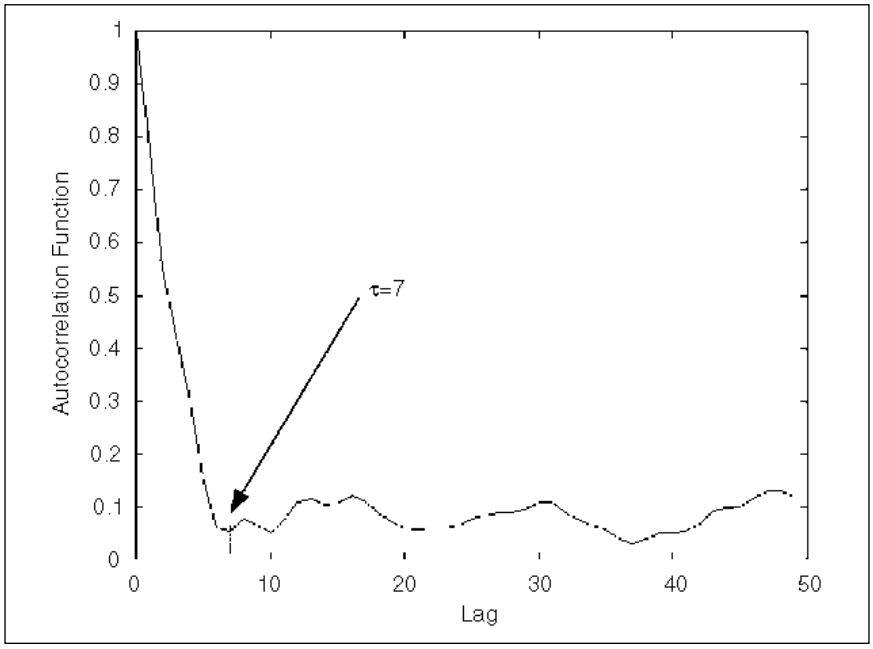

1. Selection of time delay τ using the autocovariance function.

Table 1. Values of τ for HCM and SCDHCM patients. τ was selected as the time at the first relative minimum of the autocovariance function (ACF).

HCM	τ	SCDHCM	τ
LR1	2	HR1	2
LR2	2	HR2	13
LR3	3	HR3	3
LR4	3	HR4	25
LR5	2	HR5	39
LR6	4	HR6	24
LR7	25	HR7	2
LR8	1	HR8	2

The autocovariance function (ACF) is defined by:

$$ACF(\tau) = \sum_{i=1}^{N-\tau}[(y_i - \bar{y})(y_{i+\tau} - \bar{y})]. \quad (10)$$

Table 1 shows the values of τ obtained for SCDHCM and HCM patients. As can be seen in this table, the τ values obtained from ACF vary from 1 to 39. In general, bigger values are obtained in high-risk patients (SCDHCM).

In order to obtain an accurate measure of D_c, the embedding dimension m must be at least $2D_c + 1$ [29]. Preliminary results [34] have suggested to work in an embedding dimension (m) of 20. All calculations were made using this value.

The correlation integral $C_m(r)$ is calculated for different values of r (radius of the sphere) for each embedding dimension 1 to m. From the logarithmic plot of these values (Fig. 2), the scaling region to obtain the slopes can be determined. This region is delimited by values in the y-axis. A linear regression is computed with the points contained in the scaling region for each embedding dimension. The resulting slope is the dimension $d(m)$.

In this article a new method is proposed. Using the $d(m)$ values, an exponential model of the type

$$d(m) = D_c(1 - e^{-km}) \quad (11)$$

is fitted. The values of D_c and k are estimated using the Levenberg-Marquardt method [37]. The saturation value of the curve D_c is the estimated value of the correlation dimension of the signal (Figure 3).

This is a new approach to calculate the correlation dimension. It may be more reliable than the averaging procedures normally used because the slopes of the correlation integrals, for all the different embedding dimensions m, are used at the same time. The exponential curve fit follows the asymptotic behavior of the calculated $d(m)$. Thus, it is no longer necessary to define arbitrarily where the $d(m)$ curve becomes sufficiently constant to yield a saturation value for D_c. The error calculated as the mean square root of the differences between the $d(m)$ values and the fitted curve was less than 5%, with respect to the D_c value. The Levenberg-Marquardt method was used to fit the exponential formula (11) to the $d(m)$ curve.

This methodology was tested with known mathematical models: the Lorenz model, which is chaotic; sinusoidal waves; and noise. In all cases the methodology gives expected results.

In this work, a new index is also proposed. This phenomenological index, named $D_c k$, is the product of the two parameters that characterize the fitted exponential curve, D_c and k. Geometrically, this product represents the slope of curve $d(m)$ versus m where the embedding dimension m tends to zero and, as it will be seen, it can discriminate between HCM and SCDHCM patients.

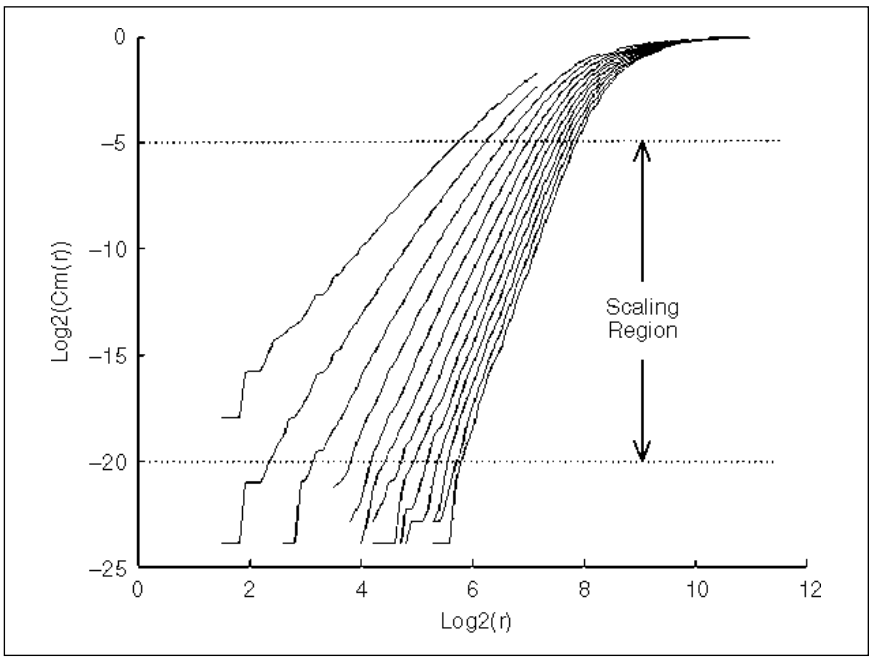

2. Correlation integral as a function of the sphere radius (*r*) for each embedding dimension showing the scaling region.

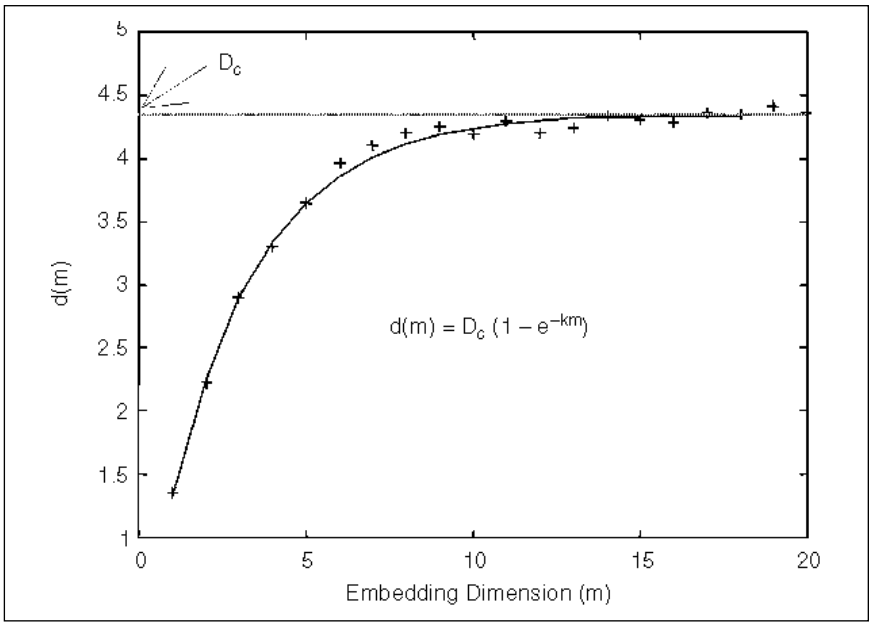

3. Correlation dimension *d* as a function of the embedding dimension *m* with a fitted exponential curve.

Results

Stationarity Analysis

The surrogate data method requires stationary data. To exclude nonstationarities from our data we divided the time series into 20 intervals of 500 samples each and compared the mean and variance of these intervals.

Hypothesizing that the observations are independent observations of a random variable z, where there is no trend, the acceptance region [28] for this hypothesis at

the $\alpha = 0.05$ level of significance is $[69 < A < 120]$ when $N_s = 20$ intervals and $[54 < A < 98]$ when $N_s = 18$ intervals.

The tachograms of LR2, LR5, LR7, LR8, and HR8 presented nonstationarities when the mean values of the segments were tested, as can be seen in Table 2. A further analysis of LR2, LR5, and LR7 time series allowed obtaining stationary data. Considering the first 18 segments of the LR2 tachogram, it could be considered stationary, with $A = 57$ calculated from the mean values and $A = 72$ calculated from the variance values. The last 18 segments were considered for tachogram LR5 obtaining $A = 56$, when studying the mean values, and $A = 59$, when studying the variance values. Tachogram LR7 was selected after the first nine intervals but considering a new $N_s = 20$ interval, because the values obtained for A were 94 when mean values were calculated and 99 when the variances were considered, both belonging to the acceptance interval.

The tachograms of patients LR8 and HR8 were removed from the analyzed data, since it was not possible to get stationary data.

Surrogate Data Method

Table 3 shows the results obtained when the surrogate data method was applied to the HRV signals of the low-risk group (HCM). Table 4 shows the results for the high-risk group (SCDHCM). For the calculation of Q_D and μ_H the correlation dimension D_C with $\tau = 1$ was used.

Table 2. Values of *A* for HCM and SCDHCM RR series, considering the mean and variance of each N_S = 20 intervals of 500 samples.

HCM	Mean (z)	Variance (z)	SCDHCM	Mean (z)	Variance (z)
LR1	106	83	HR1	89	76
LR2	58	77	HR2	113	112
LR3	111	107	HR3	119	81
LR4	89	70	HR4	105	76
LR5	56	82	HR5	79	79
LR6	118	74	HR6	70	89
LR7	51	121	HR7	105	91
LR8	69	47	HR8	36	93

Table 3. Values of correlation dimension for RR series and surrogate data from HCM low-risk group with statistical test and significance.

HCM	Q_D	μ_H	σ_H	ξ	*p*
LR1	8.3	18.9	1.92	5.52	0.017
LR2	9.6	22.6	1.20	10.80	0.006
LR3	7.9	21.4	0.75	18.0	0.0003
LR4	8.0	22.7	1.75	8.40	0.008
LR5	8.3	19.5	1.58	7.09	0.012
LR6	4.8	22.9	1.87	9.68	0.002
LR7	10.5	21.6	1.08	10.28	0.003

Table 4. Values of correlation dimension for RR series and surrogate data from SCDHCM high-risk group with statistical test and significance.

SCDHCM	Q_D	μ_H	σ_H	ξ	*p*
HR1	6.0	20.9	2.20	6.77	0.011
HR2	9.5	22.9	2.25	5.60	0.010
HR3	4.8	22.4	1.59	11.07	0.003
HR4	9.6	20.1	1.55	6.77	0.009
HR5	7.2	21.5	1.33	10.75	0.004
HR6	9.5	19.2	0.83	11.69	0.001
HR7	7.7	20.3	0.52	24.23	0.0002

All the RR series of the patients analyzed have significant differences with respect to the set of surrogate data generated.

As can be seen from the results shown in Tables 3 and 4, all the RR series of the patients analyzed have significant differences with respect to the set of surrogate data generated, and so the null hypothesis is rejected. The signals analyzed have a strong evidence of nonlinear determinism.

Correlation Dimension and $D_c k$ Index

Applying the methodology described in previous sections, D_c and $D_c k$ were calculated for the seven pairs of HCM patients. Table 5 presents the results using lag $\tau = 1$, considering the signal as a map, and Table 6 presents the results when lag τ is obtained as the first relative minimum of the autocovariance function.

Using paired-sample nonparametric techniques (Wilcoxon test), correlation dimension (D_c) does not discriminate the two groups of patients, having a mean value near 8 for both groups when using a mean value of about 8.9 when using the lag obtained from ACF. In contrast, when the $D_c k$ index is applied, the two groups are well discriminated. Significant differences were found, with $p = 0.02$ when using lag $\tau = 1$ and $p = 0.018$ when using the lag obtained from ACF.

Discussion and Conclusions

In this article a correlation dimension analysis of HRV from HCM patients with low and high risk of sudden cardiac death has been carried out. Stationarity, which is a precondition for the correlation dimension analysis, was tested, and the tachograms of two patients were rejected. The data length was a compromise between the time-series length and the stationarity. Evidence of nonlinear determinism has been tested using the surrogate data method. The results of this test clearly indicate that the null hypothesis, which states that the data comes from a linear Gaussian process, cannot be accepted and

Table 5. D_c values obtained using lag $\tau = 1$. HCM: Seven patients with low risk of sudden cardiac death. SCDHCM: Seven patients with high risk of sudden cardiac death.

HCM	D_c	$D_c k$	SCDHCM	D_c	$D_c k$
LR1	8.3	1.33	HR1	6.0	1.45
LR2	9.6	1.23	HR2	9.5	1.46
LR3	7.9	1.35	HR3	4.8	1.59
LR4	8.0	1.37	HR4	9.6	1.40
LR5	8.3	1.14	HR5	7.2	1.53
LR6	4.8	1.29	HR6	9.5	1.39
LR7	10.5	1.04	HR7	7.7	1.50
Mean ± sd	8.2 ± 1.8	1.25 ± 0.12	Mean ± sd	7.9 ± 1.8	1.47 ± 0.07

Table 6. D_c values, using a lag τ corresponding to the first relative minimum of ACF. HCM: Seven patients with low risk of sudden cardiac death. SCDHCM: Seven patients with high risk of sudden cardiac death. sd = standard deviation.

HCM	τ	D_c	$D_c k$	SCDHCM	τ	D_c	$D_c k$
LR1	2	8.2	1.42	HR1	2	7.1	1.45
LR2	2	9.5	1.27	HR2	13	8.3	1.48
LR3	3	8.8	1.46	HR3	3	7.5	1.54
LR4	3	10.4	1.43	HR4	25	9.7	1.51
LR5	2	10.6	1.28	HR5	39	10.2	1.47
LR6	4	5.1	1.43	HR6	24	9.2	1.55
LR7	25	10.8	1.08	HR7	2	10.0	1.46
Mean ± sd		9.0 ± 2.0	1.34 ± 0.14	Mean ± sd		8.9 ± 1.2	1.49 ± 0.04

then the nonlinear nature of these HRV signals can be concluded.

Regarding the methodology used to compute the correlation dimension, an exponential fit to obtain this value has been proposed. This procedure seems to be a better approach to obtain the value of the dimension, since it uses all the points of the $d(m)$ curve and defines the correlation dimension as an asymptotic value obtained with increasing embedding.

From the results obtained analyzing these HCM patients, it can be seen that the correlation dimension does not separate the groups of low- and high-risk for sudden cardiac death. The averaged D_c in both groups is very similar for the lag $\tau = 1$ and also for the lag determined using the ACF. However, a careful inspection of the obtained results with the proposed methodology suggests that the product of D_c by k (exponential constant) can discriminate the two groups. Although the group of patients studied here is small, clear differences are obtained between the low-risk and high-risk groups. This phenomenological index, named here $D_c k$, geometrically represents the slope of the curve of dimension $d(m)$, when m tends to zero. Further analyses are needed to understand the interpretation of this phenomenological index.

Acknowledgments

This work was partially financed by grant CICYT (TIC2001-2167-C02-01) from the Spanish Government, KBN grant 2P03B-020-09 from the Polish Government, the National Council for Science and Technology (CONACYT) from Mexico, and the European Society of Cardiology.

Raul Carvajal received his B.S. in biology in 1986 from the National University of Mexico (UNAM). He received his M.Sc. in computer sciences from the Postgraduate College of Mexico in 1993 and his Ph.D. degree in biomedical engineering from the Technical University of Catalonia (UPC), Barcelona, Spain, in 1999. Currently he is a professor at the Faculty of Computer Sciences of the University of Sinaloa (UAS) at Mazatlan, Mexico. His interests include modeling and simulation of biological systems and nonlinear analysis of biomedical signals.

Jan J. Zebrowski received his M.S.E.E. in applied physics from the Warsaw University of Technology in 1974, was a graduate student (special status) at Applied Physics, Caltech, from 1977-1979, and received Ph.D.s in solid state physics and in physics at the Warsaw University of Technology in 1981 and 1989, respectively. He obtained the title of professor in physics (given by the state of Poland) in 2001. He holds a permanent position of Professor Extraordinary at the Warsaw University of Technology and is head of the Department of Theory of Magnetism and Phase Transitions at the Faculty of Physics, WUT. His main interests are analysis of nonstationary states of dynamical systems, applications of chaos theory to medical diagnostics, and modeling of the heart and of the cardiovascular system.

Montserrat Vallverdú received her M.S. degree in electrical engineering and her Ph.D. degree in bioengineering at the Technical University of Catalonia, Barcelona, Spain, in 1986 and 1993, respectively. Since 1986 she has been a research member at the Cybernetics Institute working on bioengineering. Dr. Vallverdú has been a research member and an assistant professor at the Biomedical Engineering Research Centre, Technical University of Catalonia, since 1997. Her research interests focus on complexity and time-frequency analysis for the recovery of clinically useful hidden information in cardiac and respiratory signals.

Rafa Baranowski graduated from the Academy of Medicine, Warsaw, Poland, in 1986. He received his Ph.D. in medicine in 1993 and his Ph.D. in cardiology in 2000 at the National Institute of Cardiology, Warsaw. There he is the head of the 24-hour ECG Monitoring Lab. His scientific interests center on the analysis of heart-rate variability and of repolarization processes in the heart by classical and nonlinear methods (including symbolic dynamics), with particular emphasis on gender differences and on the risk of cardiac arrest.

Pere Caminal received his M.S. and Ph.D. degrees in mechanical engineering from the Technical University of Catalonia (UPC), Barcelona, Spain, in 1974 and 1980, respectively. Currently, he is a professor of Automatic Control in the Department of Control Engineering at the same university. He is also director of the master's program in biomedical engineering (UPC). His interests include modeling and simulation of biological systems and biomedical signal processing.

Address for Correspondence: Dr. Pere Caminal, ESAII Department, Universitat Politècnica de Catalunya, Pau Gargallo 5, 08028, Barcelona, Spain. E-mail: caminal@creb.upc.es. Fax: +34 93-401.70.45. Tel.: +34 93-401.71.60

References

[1] Hypertrophic Cardiomyopathy Association, 1999. http:// www.kanter.com/hcm/

[2] P. Richardson, W. McKenna, M. Bristow, B. Maisch, B. Mautner, J.B. O'Connel, J. Olsen, G. Thiene, J. Goodwin, I. Gyarfas, I. Martin, and P. Nordet, "Report of the 1995 WHO/ISFC task force on the definition and classification of cardiomyopathies," *Circulation*, vol. 93, pp. 841-842, 1996.

[3] B.J. Maron, F. Cecchi, and W.J. McKenna, "Risk factors and stratification for sudden cardiac death in patients with hypertrophic cardiomyopathy," *Br. Heart J.*, vol. 72, pp. 13-18, 1994.

[4] R. Baranowki, W. Poplawska, M. Vallverdú, L. Chojnowska, E. Orlowska, W. Rydlewska-Sadowska, P. Caminal, and A. Bayés de Luna, "Analysis of QTc in 24-hour ECG," *Folia Cardiologica*, vol. 6, pp. 338-346, 1999.

[5] F. Clariá, M. Vallverdú, R. Baranowski, L. Chojnowska, and P. Caminal, "Time-frequency analysis of the RT and RR variability to stratify hypertrophic cardiomyopathy patients," *Comput. Biomed. Res.*, vol. 33, pp. 416-430, 2000.

[6] Task Force of the European Society of Cardiology and the North American Society of Pacing and Electrophysiology, "Heart rate variability—Standards of measurement, physiological interpretation and clinical use," *Circulation*, vol. 93, pp. 1043-1065, 1996.

[7] G. Baselli, S. Cerutti, S. Civardi, F. Lombardi, A. Malliani, M. Merri, M. Pagani, and G. Rizzo, "Heart rate variability signal processing: A quantitative approach as an aid to diagnosis in cardiovascular pathologies," *Int. J. Bio-Med. Comput.*, vol. 20, pp. 51-55, 1987.

[8] A. Voss, J. Kurths, H.J. Kleiner, A. Witt, N. Wessel, P. Saparin, K.J. Osterziel, R. Schurath, and R. Dietz, "The application of methods of non-linear dynamics for the improved and predictive recognition of patients threatened by sudden cardiac death," *Cardiovascular Res.*, vol. 31, pp. 419-433, 1996.

[9] A.M. Bianchi, L.T. Mainardi, C. Meloni, S. Chierchi, and S. Cerutti, "Continuous monitoring of the sympatho-vagal balance through spectral analysis," *IEEE Eng. Med. Biol. Mag.*, vol. 16, pp. 64-73, 1997.

[10] J. Haaksma, W.A. Dijk, J. Brouwer, M.P. Van Der Berg, B. Mulder, and H.J. Crijns, "The influence of recording lengths on time and frequency domain analysis of heart rate variability," *Comput. Cardiology*, vol. 25, pp. 377-380, 1998.

[11] B.J. West, A.L. Goldberger, G. Rouner, and V. Bhargava, "Nonlinear dynamics of the heartbeat I. The A.V. junction: Passive conduit or active oscillator," *Physica D*, vol. 17, pp. 198-206, 1985.

[12] S.R. Chialvo and J. Jalife, "Non-linear dynamics of cardiac excitation and impulse propagation," *Nature*, vol. 330, pp. 749-752, 1987.

[13] J.B. Bassingthwaighte and J.H.G.M. Van Beek, "Lightning and the heart: Fractal behavior in cardiac function," *Proc. IEEE*, vol. 76, pp. 693-699, 1988.

[14] A.L. Goldberger, D.R. Rigney, and B.J. West, "Chaos and fractals in human physiology," *Sci. Amer.*, vol. 262, pp. 42-49, 1990.

[15] D.T. Kaplan, M.L. Furman, S. Pincus, S.M. Ryan, L.A. Lipsitz, and A.L. Goldberger, "Aging and the complexity of cardiovascular dynamics," *Biophys. J.*, vol. 59, pp. 945-949, 1991.

[16] R. Baranowski, J.J. Zebrowski, W. Poplawska, M.A. Mañanas, R. Jané, P. Caminal, L. Cojnowska, W. Rydlewska-Sadowska, X. Viñolas, J. Guindó, and A. Bayes de Luna, "3-dimensional Poincaré plots of the QT intervals—An approach to nonlinear QT analysis," *Comput. Cardiology*, vol. 22, pp. 789-792, 1995.

[17] J.J. Zebrowski, T. Buchner, R. Baranowski, and W. Poplawska, "Nonlinear analysis of heart dynamics," *Med. Biol. Eng. Comput.*, vol. 34, pp. 379-380, 1996.

[18] J.J. Zebrowski, W. Poplawska, R. Baranowski, and T. Buchner, "Nonlinear analysis, theory, methods and applications," in *Proc. 2nd World Congr. Nonlinear Analysis*, vol. 30, pp. 1007-1017, 1997.

[19] J.J. Zebrowski, W. Poplawska, R. Baranowski, and T. Buchner, "Measuring the complexity of non-stationary times series—Nonlinear interpretations of selected physiological processes," *Acta Phys. Pol.*, vol. B30, pp. 2547-2570, 1999.

[20] T.J. Bigger, R.C. Steinman, L.M. Rolnitzky, J.L. Fleiss, P. Albrecht, and R.J. Cohen, "Power law behavior of RR interval variability in healthy middle aged persons, patients with recent acute myocardial infarction and patients with heart transplant," *Circulation*, vol. 93, pp. 2142-2151, 1996.

[21] F. Lombardi, G. Sandrone, A. Mortara, D. Torzillo, M.T. La Rovere, M.G. Signorini, S. Cerutti, and S. Malliani, "Linear and nonlinear dynamics of heart rate variability after acute myocardial infarction with normal and reduced left ventricular ejection fraction," *Am. J. Cardiol.*, vol. 77, pp. 1283-1288, 1996.

[22] N. Wessel, A. Voss, J. Kurths, A. Schirdewan, K. Hnatkowa, and M. Malik, "Evaluation of renormalized entropy for risk stratification using heart rate variability data," *Med. Biol. Eng. Comput.*, vol. 38, pp. 380-685, 2000.

[23] N.B. Abraham, A.M. Albano, A. Passamante, P.E. Rapp, and R. Gilmore, "Complexity and chaos," *Int. J. Bifur. Chaos*, vol. 3, pp. 485-490, 1993.

[24] H. Kantz and T. Schreiber, *Nonlinear Time Series Analysis*. Cambridge, U.K.: Cambridge Univ. Press, 1997.

[25] J. Theiler, S. Eubank, A. Longtin, B. Galdrikian, and D. Farmer, "Testing for nonlinearity in time series: The method of surrogate data," *Physica D*, vol. 58, pp. 77-94, 1992.

[26] P. Laguna, R. Jané, and P. Caminal, "Automatic detection of wave boundaries in multilead ECG signals: Validation with the CSE database," *Comput. Biomed. Res.*, vol. 27, pp. 45-60, 1994.

[27] F. Clariá, M. Vallverdú, R. Baranowski, L. Chonowska, P. Martínez, and P. Caminal, "Time-frequency representation of the HRV: A tool to characterize sudden cardiac death in hypertrophy cardiomyopathy patients," in *Proc. 22nd Annu. Int. Conf. IEEE Engineering in Medicine and Biology Society, Chicago, IL*, CD-ROM, 2000.

[28] J.S. Bendat A.G. and Piersol, *Random Data. Analysis and Measurement Procedures*. New York: Wiley-Interscience, 1986.

[29] F. Takens, "Detecting strange attractors in turbulence," in *Dynamical Systems and Turbulence, Lecture Notes in Math*, D.A. Rand and L.S. Young, Eds. Berlin, Germany: Springer-Verlag, 1981, pp. 366-381.

[30] P. Grassberger and I. Procaccia, "Measuring the strangeness of strange attractors," *Physica D*, vol. 9, pp. 189-208, 1983.

[31] M. Ding, C. Grebogi, E. Ott, T. Sauer, and J.A. Yorke, "Estimating correlation dimension from chaotic time series: When does plateau occur?," *Physica D*, vol. 69, pp. 404-424, 1993.

[32] T.M. Kruel and A. Freund. (1991). "SCOUNT, A program to calculate the correlation and information dimension from attractors by the method of sphere-counting." Available: http://inls.ucsd.edu/ftp/pub/

[33] J. Theiler, "Spurious dimension from correlation algorithms applied to limited time series data," *Phys. Rev. A.*, vol. 34, pp. 2427-2432, 1986.

[34] R. Carvajal, M. Vallverdú, R. Baranowski, J.J. Zebrowski, and P. Caminal, "Correlation dimension of HRV to stratify HCM-patients," *Elektofizjologia i Stymulacja Serca*, vol. 4, p. 7, 1997.

[35] R. Castro and T. Sauer, "Correlation dimension of attractors through interspike intervals," *Phys. Rev. E*, vol. 55, pp. 287-290, 1997.

[36] G.P. King, R. Jones, and D.S. Broomhead, "Phase portraits from a time series: A singular system approach," *Nucl. Phys.*, vol. B2, p. 379, 1987.

[37] J.J. Moré, "The Levenberg-Marquardt algorithm: Implementation and theory," in *Lecture*

cated by an arrow, is outside the detected cerebral cortical border. Although the defect should be anatomically included inside the cortical border, the low intensity of the lesion classifies it as the background area. Therefore, for the correct analysis of cerebral cortical blood flow, the cerebral cortical border has to be modified. A refinement step is presented in the following subsection.

The Refinement of the Outer Border of the Cerebral Cortex

The aim of this step is to refine the outer cerebral cortical border. We make use of the head object border (denoted as B_A), the initial outer cerebral cortical border (denoted as B_B), and the distance code transformation to obtain the correct outer cerebral border. Anatomically, in a HMPAO slice, the head border and the outer cerebral cortical border are analog in shape to each other. So, the distance code between the two borders can be regarded as close to a fixed value. Based on this assumption, distance transformation [15]-[17] is applied in the refinement of the border B_B. Distance transformation (DT), which is widely used in image processing and computer vision, can convert an image of black and white pixels to an imagewhere each pixel has a value (i.e., distance code) representing the distance to the nearest border pixel. The refinement approach can be divided into the following steps:

Step 1: Distance transformation is performed with respect to the head object border B_A. The average distance code, denoted as AVDC, of every pixel on border B_B is calculated.

Step 2: Pixels on the border B_B with the distance code greater than 1.5*AVDC were grouped as the defect seed pixels [see Figure 5(d)].

Step 3: The seed pixels begin to grow if the grown pixel is outside the border B_B and its distance code is larger than AVDC. This region grow step is repeated until no further pixels can be added to the defect region [see Figure 5(e)].

Step 4: The pixels inside the border B_B and the grown pixels are grouped together to form a new region. The boundary of the new region is the refined outer cerebral cortical border (denoted as B_C).

For the image shown in Figure 5(a), the border B_C is shown in Figure 5(f). It is observed that border B_B and border B_C are almost identical except that the defect region is inside the border B_C. For the normal case, the border B_C is the same as the border B_B because no defect region is included. That is, the refinement approach only refines the border with abnormality, and it can exclude the effect of disease lesion and extract the border successfully.

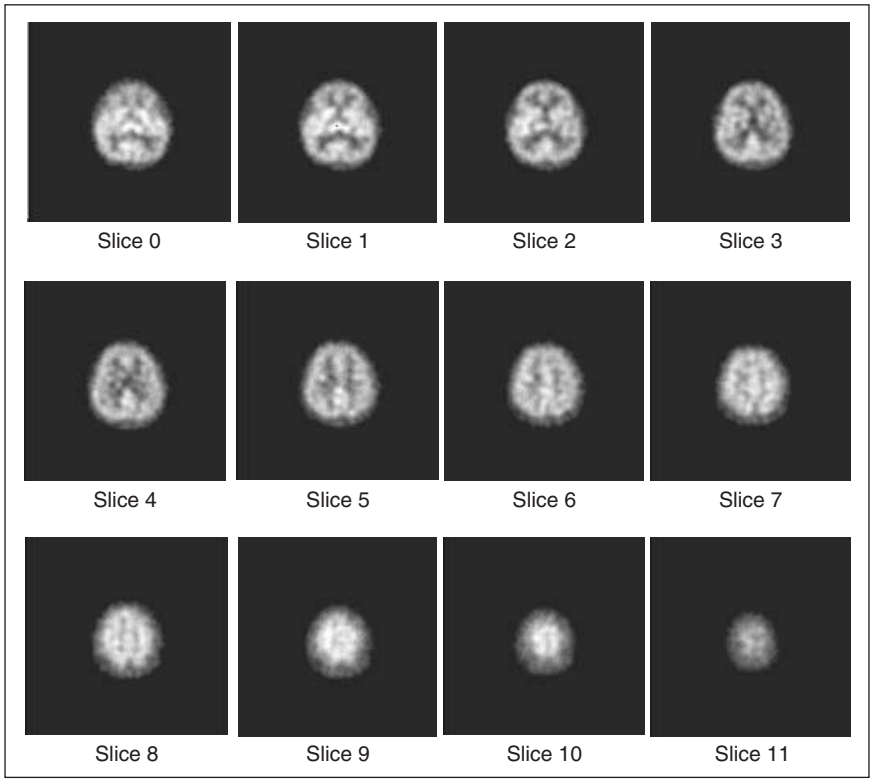

2. A series of 12 HMPAO brain SPECT images.

Extracting the Cerebral Cortical Region

The aim of this step is to obtain the cerebral cortical region based on the resulting cerebral cortical border. First, DT is performed with respect to the border B_C. Second, the pixels inside the border B_C and with distance codes less than *Tk* are grouped to the cerebral cortical region. The value of *Tk* (the thickness of the cerebral cortex) is determined and given by the doctor empirically.

For the image shown in Figure 4(a), Figure 4(f) shows the resulting cerebral cortical region with an employed *Tk* value of 5. The pixel values in the cerebral cortical region are then used to generate the bullseye display.

Bullseye Display

Bullseye Display Format

The goal of this display method is to integrate the cerebral cortical region of an entire study into a single functional image (bullseye plot). Figure 6 shows the schematic representation of the bullseye methodology. In Figure 6(a), the data source consists of a series of n HMPAO brain SPECT ($S_0, S_1, ..., S_{n-1}$) images. These images were selected from the base slice (S_0) that was positioned at 3.5 cm above the CM line and extended to the top slice (S_{n-1}) of the head by the doctor. In each image, the cerebral cortical region was extracted first. In Figure 6(b), the bullseye plot consists of n concentric rings ($R_0, R_1, ..., R_{n-1}$) with progressive increment in diameter. The outer ring is denoted as R_0, and the inner ring is denoted as R_{n-1}. Each ring is divided into 40 sectors. The

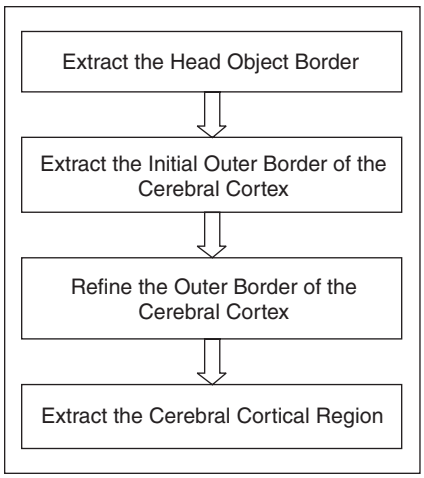

3. Flowchart for segmentation of cerebral cortical region.

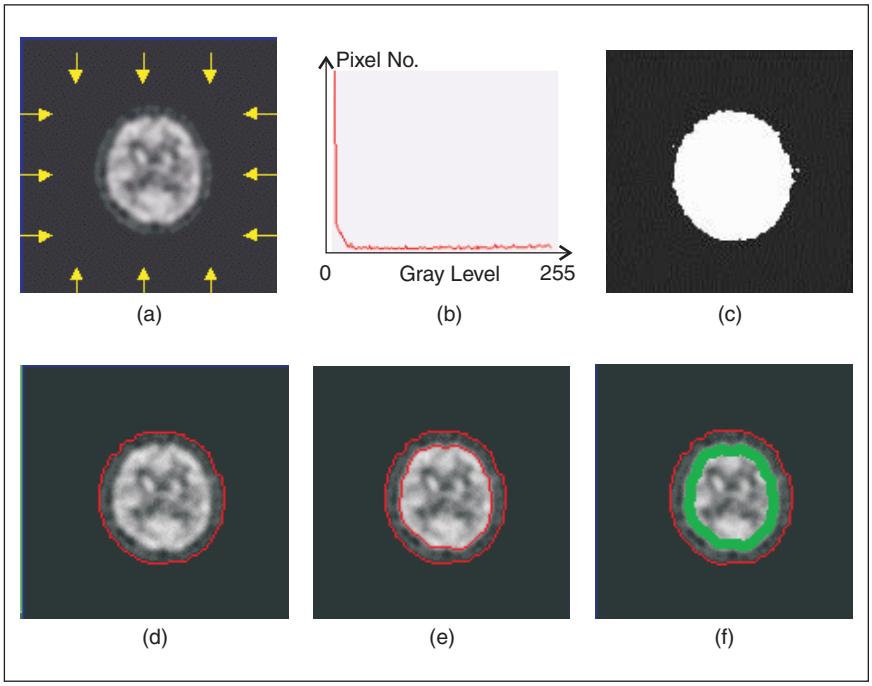

4. (a) Normal HMPAO brain SPECT and scan lines. (b) Smoothed histogram. (c) Resulting image after the scanning method with threshold L_t. (d) Morphologically smoothed head border overlapped with the original image. (e) Outer cerebral cortical border with threshold H_t applied. (f) Cerebral cortical region.

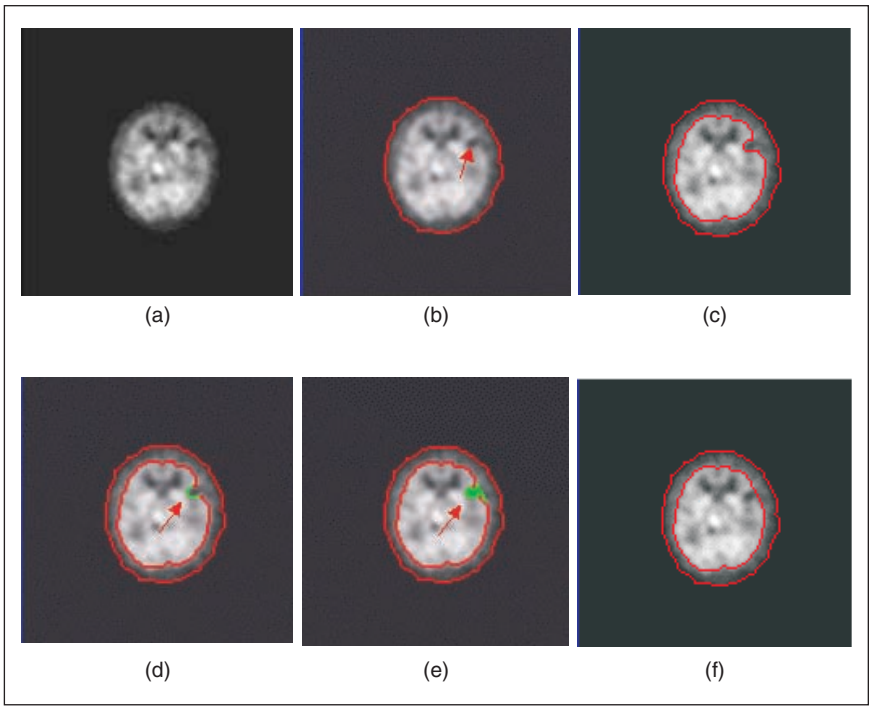

5. (a) Abnormal HMPAO brain SPECT. (b) Head object border B_A. (c) Detected outer cerebral cortical border B_B with defect indicated by an arrow. (d) Seed region (green points). (e) Detected defect region (green points). (f) Refined outer cerebral cortical border B_C.

ring R_i records the information of the cerebral cortical region in S_i. The cerebral cortical region in S_i is also divided into 40 regions. The information of the jth section of S_i is stored in the corresponding jth sector of R_i. Figure 7 illustrates the relationship between the cerebral cortical region in S_i and the ring R_i. All sectors on the bullseye plot are then assigned with specified colors to illustrate the function distribution of the whole brain.

Color Determination of Each Sector in the Bullseye Plot

In the bullseye display, each sector corresponds to a specific brain region and is assigned with a certain color index. The color index determines the RGB values in each sector. In our system, the ratio of the radioactivities of the each section in the cerebral cortex to the radioactivities in the reference region (here the cerebellum region) is used to determine the color index of each sector in the bullseye plot. Figure 8 shows that the reference region is manually defined as a rectangular region. The average gray level of pixels in the reference region (denoted as RG) is calculated. The average gray level of pixels in the jth region of the cerebral cortical region in slice S_i is also calculated and is denoted as $G_{i,j}$. The color index for the jth sector of the ring R_i can be obtained by the following equation:

$$\text{Index}_{i,j} = [(G_{i,j} / RG) \times RG_{\text{index}}],$$

where RG_{index} is the color index for the reference region and is set to 200 in our study. The RGB values used for each sector in the bullseye map are determined according to its color index. Figure 9(a) shows the schema to obtain the corresponding RGB values of each color index. This approach adopts color composition as a function of R (red), G (green), and B (blue). In Figure 9(a), the coordinates (R, G) of points A, B, and C are (230, 25), (50, 205), and (0, 0), respectively. The A→B path is equally sampled with 128 points, and the B→C path is also equally sampled with 128 points. That is, there are 256 points sampled in the A→B→C path. For each sampled point, the values of R and G can be computed by using the linear interpolation method. For the values of R and G, the corresponding value of B (blue) is obtained from the equation $R+G+B=255$. In the bullseye plot, the color values $(R_{(i)}, G_{(i)}, B_{(i)})$ are assigned to the sector with color index i, where $(R_{(i)}, G_{(i)})$ is the coordinate of the ith sampled point in the

cated by an arrow, is outside the detected cerebral cortical border. Although the defect should be anatomically included inside the cortical border, the low intensity of the lesion classifies it as the background area. Therefore, for the correct analysis of cerebral cortical blood flow, the cerebral cortical border has to be modified. A refinement step is presented in the following subsection.

The Refinement of the Outer Border of the Cerebral Cortex

The aim of this step is to refine the outer cerebral cortical border. We make use of the head object border (denoted as B_A), the initial outer cerebral cortical border (denoted as B_B), and the distance code transformation to obtain the correct outer cerebral border. Anatomically, in a HMPAO slice, the head border and the outer cerebral cortical border are analog in shape to each other. So, the distance code between the two borders can be regarded as close to a fixed value. Based on this assumption, distance transformation [15]-[17] is applied in the refinement of the border B_B. Distance transformation (DT), which is widely used in image processing and computer vision, can convert an image of black and white pixels to an imagewhere each pixel has a value (i.e., distance code) representing the distance to the nearest border pixel. The refinement approach can be divided into the following steps:

Step 1: Distance transformation is performed with respect to the head object border B_A. The average distance code, denoted as AVDC, of every pixel on border B_B is calculated.

Step 2: Pixels on the border B_B with the distance code greater than 1.5*AVDC were grouped as the defect seed pixels [see Figure 5(d)].

Step 3: The seed pixels begin to grow if the grown pixel is outside the border B_B and its distance code is larger than AVDC. This region grow step is repeated until no further pixels can be added to the defect region [see Figure 5(e)].

Step 4: The pixels inside the border B_B and the grown pixels are grouped together to form a new region. The boundary of the new region is the refined outer cerebral cortical border (denoted as B_C).

For the image shown in Figure 5(a), the border B_C is shown in Figure 5(f). It is observed that border B_B and border B_C are almost identical except that the defect region is inside the border B_C. For the normal case, the border B_C is the same as the border B_B because no defect region is included. That is, the refinement approach only refines the border with abnormality, and it can exclude the effect of disease lesion and extract the border successfully.

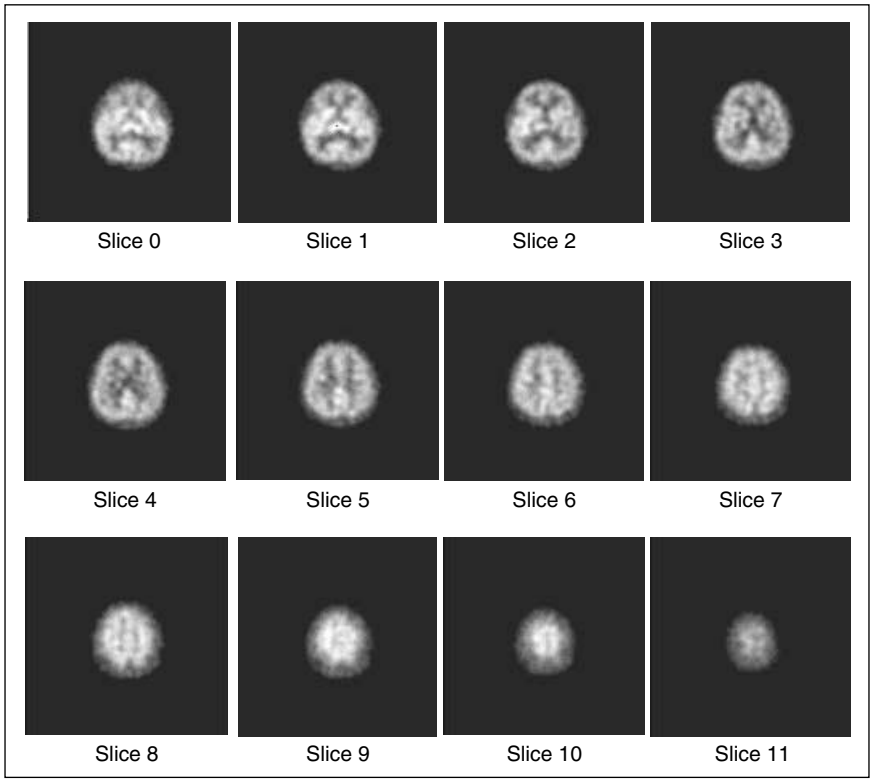

2. A series of 12 HMPAO brain SPECT images.

Extracting the Cerebral Cortical Region

The aim of this step is to obtain the cerebral cortical region based on the resulting cerebral cortical border. First, DT is performed with respect to the border B_C. Second, the pixels inside the border B_C and with distance codes less than *Tk* are grouped to the cerebral cortical region. The value of *Tk* (the thickness of the cerebral cortex) is determined and given by the doctor empirically.

For the image shown in Figure 4(a), Figure 4(f) shows the resulting cerebral cortical region with an employed *Tk* value of 5. The pixel values in the cerebral cortical region are then used to generate the bullseye display.

Bullseye Display

Bullseye Display Format

The goal of this display method is to integrate the cerebral cortical region of an entire study into a single functional image (bullseye plot). Figure 6 shows the schematic representation of the bullseye methodology. In Figure 6(a), the data source consists of a series of n HMPAO brain SPECT ($S_0, S_1, ..., S_{n-1}$) images. These images were selected from the base slice (S_0) that was positioned at 3.5 cm above the CM line and extended to the top slice (S_{n-1}) of the head by the doctor. In each image, the cerebral cortical region was extracted first. In Figure 6(b), the bullseye plot consists of n concentric rings ($R_0, R_1, ..., R_{n-1}$) with progressive increment in diameter. The outer ring is denoted as R_0, and the inner ring is denoted as R_{n-1}. Each ring is divided into 40 sectors. The

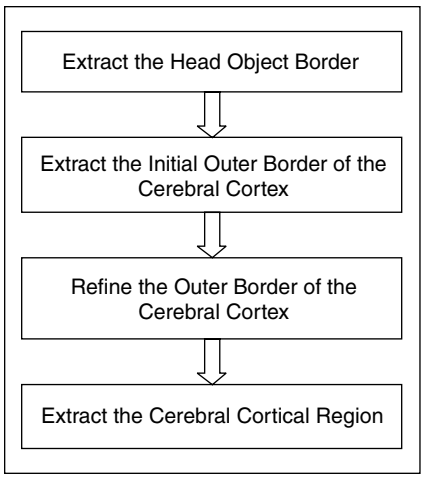

3. Flowchart for segmentation of cerebral cortical region.

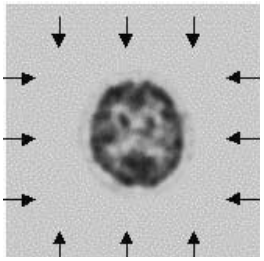

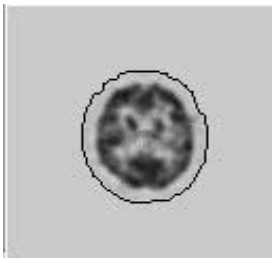

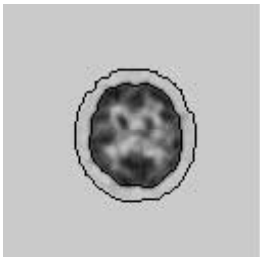

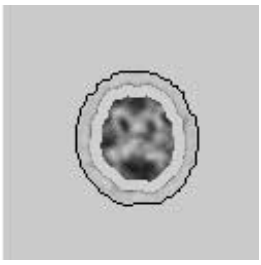

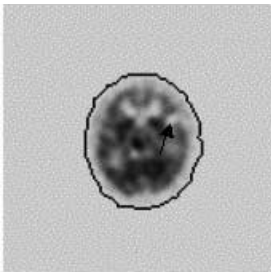

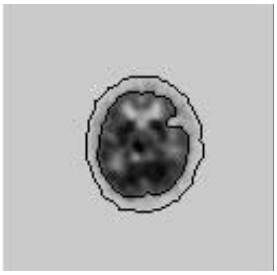

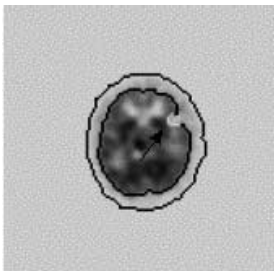

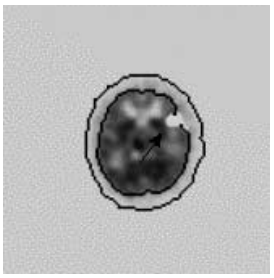

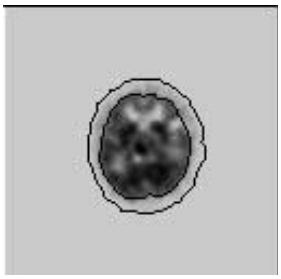

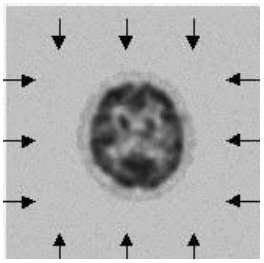

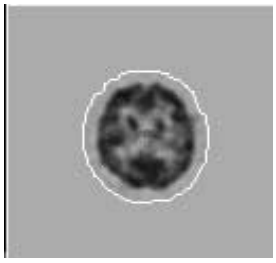

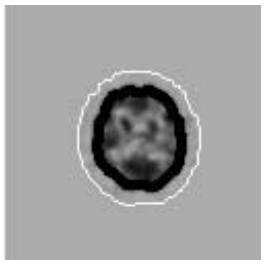

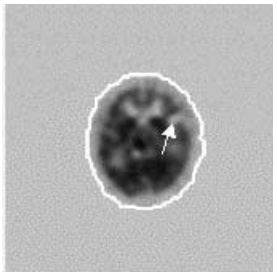

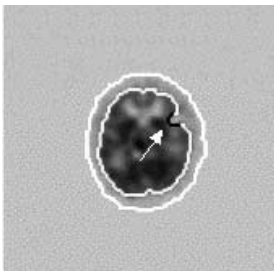

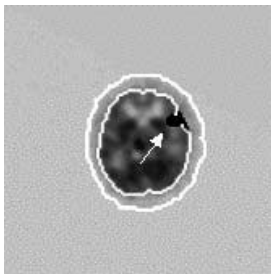

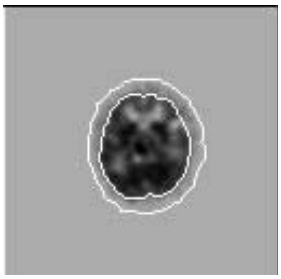

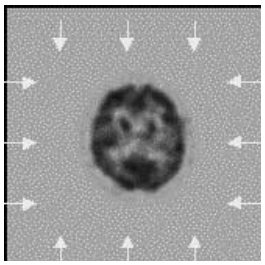

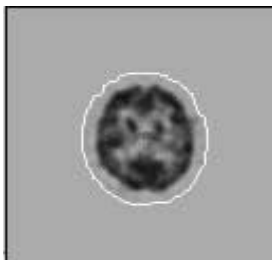

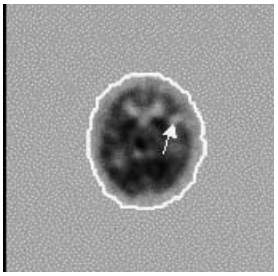

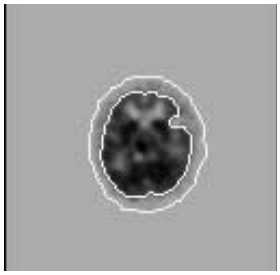

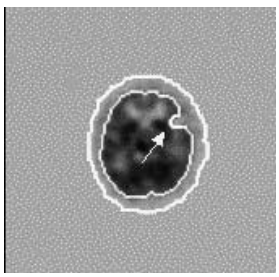

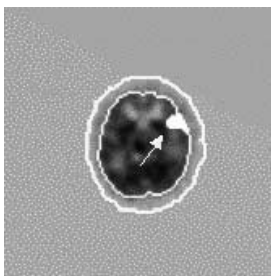

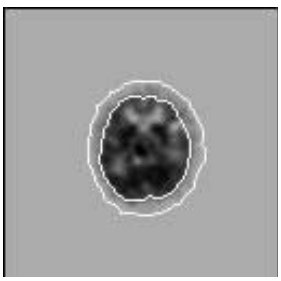

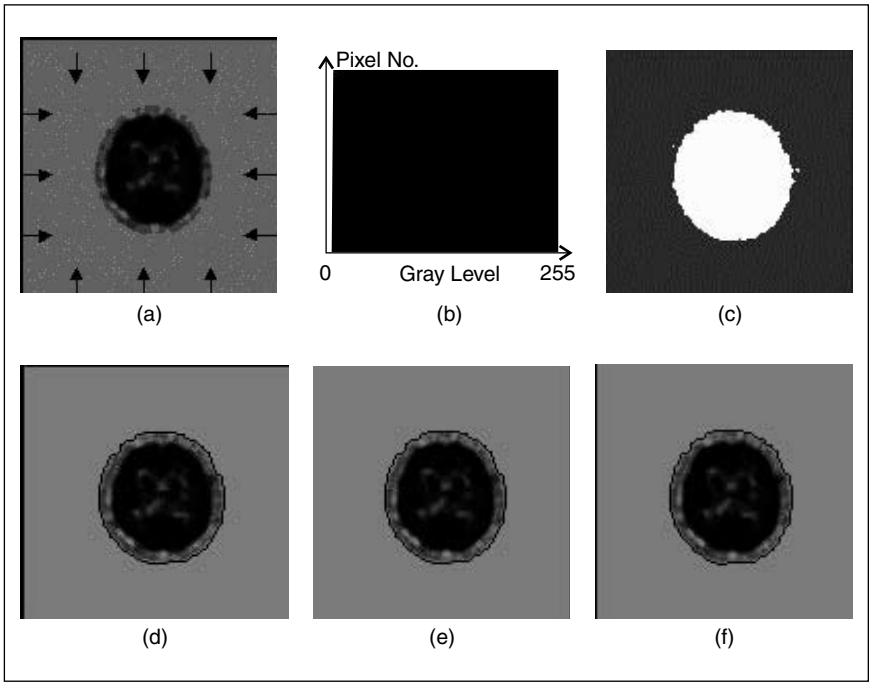

4. (a) Normal HMPAO brain SPECT and scan lines. (b) Smoothed histogram. (c) Resulting image after the scanning method with threshold L_t. (d) Morphologically smoothed head border overlapped with the original image. (e) Outer cerebral cortical border with threshold H_t applied. (f) Cerebral cortical region.

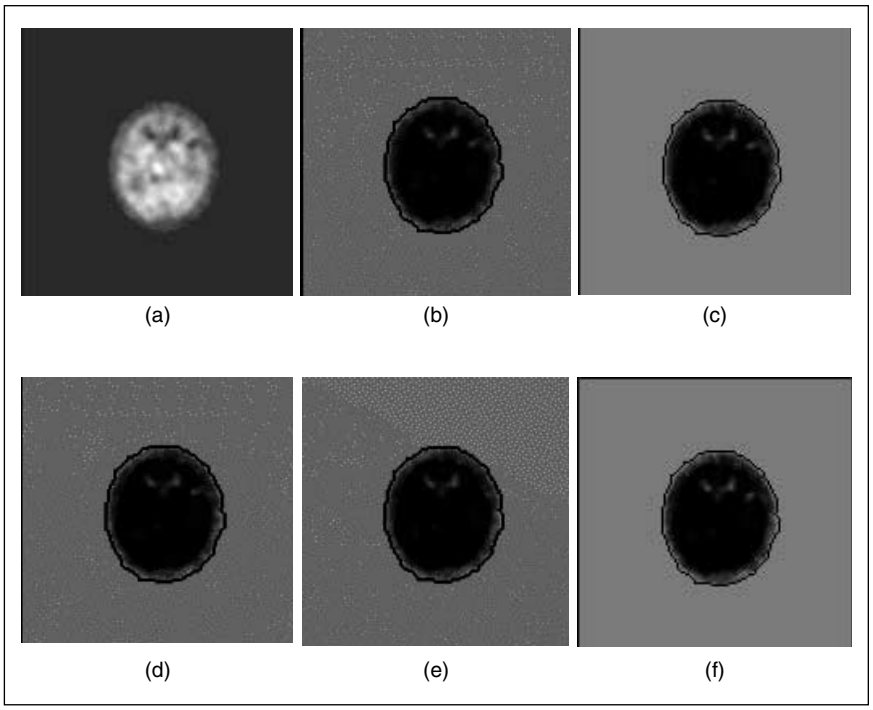

5. (a) Abnormal HMPAO brain SPECT. (b) Head object border B_A. (c) Detected outer cerebral cortical border B_B with defect indicated by an arrow. (d) Seed region (green points). (e) Detected defect region (green points). (f) Refined outer cerebral cortical border B_C.

ring R_i records the information of the cerebral cortical region in S_i. The cerebral cortical region in S_i is also divided into 40 regions. The information of the *j*th section of S_i is stored in the corresponding *j*th sector of R_i. Figure 7 illustrates the relationship between the cerebral cortical region in S_i and the ring R_i. All sectors on the bullseye plot are then assigned with specified colors to illustrate the function distribution of the whole brain.

Color Determination of Each Sector in the Bullseye Plot

In the bullseye display, each sector corresponds to a specific brain region and is assigned with a certain color index. The color index determines the RGB values in each sector. In our system, the ratio of the radioactivities of the each section in the cerebral cortex to the radioactivities in the reference region (here the cerebellum region) is used to determine the color index of each sector in the bullseye plot. Figure 8 shows that the reference region is manually defined as a rectangular region. The average gray level of pixels in the reference region (denoted as *RG*) is calculated. The average gray level of pixels in the *j*th region of the cerebral cortical region in slice S_i is also calculated and is denoted as $G_{i,j}$. The color index for the *j*th sector of the ring R_i can be obtained by the following equation:

$$\text{Index}_{i,j} = [(G_{i,j} / RG) \times RG_{\text{index}}],$$

where RG_{index} is the color index for the reference region and is set to 200 in our study. The RGB values used for each sector in the bullseye map are determined according to its color index. Figure 9(a) shows the schema to obtain the corresponding RGB values of each color index. This approach adopts color composition as a function of R (red), G (green), and B (blue). In Figure 9(a), the coordinates (*R*, *G*) of points A, B, and C are (230, 25), (50, 205), and (0, 0), respectively. The A→B path is equally sampled with 128 points, and the B→C path is also equally sampled with 128 points. That is, there are 256 points sampled in the A→B→C path. For each sampled point, the values of *R* and *G* can be computed by using the linear interpolation method. For the values of *R* and *G*, the corresponding value of *B* (blue) is obtained from the equation *R*+*G*+*B*=255. In the bullseye plot, the color values $(R_{(i)}, G_{(i)}, B_{(i)})$ are assigned to the sector with color index *i*, where $(R_{(i)}, G_{(i)})$ is the coordinate of the *i*th sampled point in the

A→B→C path. Figure 9(b) shows the color palette for each color index. It is observed that red region indicates the higher color index and blue region indicates the lower color index

Experimental Studies

We utilized the bullseye display in patients with various neuropsychologic disorders to evaluate its clinical usefulness. Figure 10(a) shows a SPECT study obtained in a patient with sudden onset of palinopsia due to cerebrovascular disease. Markedly decreased perfusion in the territory of the occluded cerebral artery was well demonstrated. We found that the bullseye display is helpful in identifying which artery is involved in cerebrovascular disease because of its distinct manifestation of different territory of each major cerebral artery.

In a boy referred for evaluation of chronic motor and vocal tics, changes of cerebral blood flow in the frontal areas are shown by bullseye [Figure 10(b)]. We also observed some characteristic bullseye patterns in certain diseases. For example, in different types of dementia, bullseye has different manifestations [Figure 10(c) and (d)], so it is valuable for diagnosis of dementia.

The diseased areas can be well demonstrated on the bullseye display; however, the 3-D spatial information on a 3-D head model is not yet available. Although SPECT images have been prepared in all the cases of clinical applications, few corresponding MR images can be used for image registration and demonstration. In other words, we can hardly obtain both SPECT and MR images from a regular patient. In 3-D visualization, we propose to register the SPECT image with respect to a 3-D MR head model, which is an ordinary 3-D MR image volume. This model includes two components: the first component is the 3-D head surface and the second component is the correspondence relation between each sector in the bullseye plot and 3-D region on the head model surface. Since the bullseye display is in a defined format, each sector can correspond approximately to a specific region of the head model. After the sector reflecting the low radioactivity was selected in the bullseye plot, the head surface and the diseased regions can be visualized simultaneously in 3-D without additional MR images and registration process required.

By aligning [18] HMPAO SPECT with model MRI images, lesions demonstrated on bullseye can also be shown on MRI to help localization. Figure 11 demonstrates the geometrical relationship between the 3-D head model and the defect depicted on the bullseye display. In Figure 11(b), the sectors reflecting abnormal function were visualized together with the 3-D head surface simultaneously. The semi-boundary display method [19] was applied for visualization. Figure 11(b)-(d) shows the results in three different views. These results can provide better 3-D perception of the diseased region for physicians and patients to understand the geometrical condition of lesions.

Conclusions and Further Research

In this article we have developed a computer-aided diagnosis system for the detection and visualization of brain lesions in the cerebral cortex. In this system, a hybrid method, combining gray-level thresholding and distance code discrimination, is proposed to obtain the cerebral cortical region. The pixel values of HMPAO SPECT in the cerebral cortical region were then visualized by the bullseye display. The interpretation of the bullseye display is more efficient and effective to illustrate the global function distribution of the brain than that of the conventional multiframe display. This adopted display method synthesizes all the SPECT brain images into a single reproducible functional image that can be objectively reviewed and that serves to point out abnormalities for further review. We also provide the 3-D visualization by displaying the selected lesions in reference to a general head model obtained from MR images. This capability helps to visualize the approximated position of the lesion in 3-D geometry. Many experimental results have shown that the system is

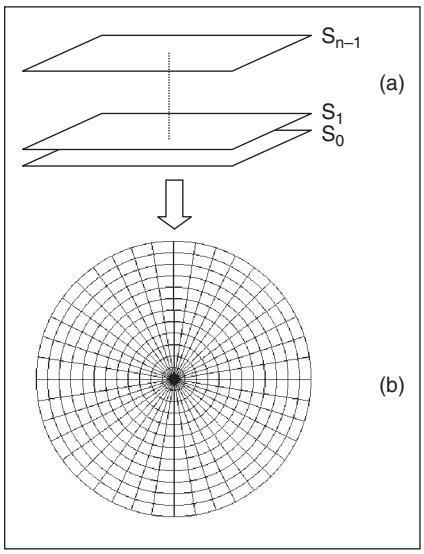

6. Schematic representation of bullseye methodology. (a) A series of HMPAO brain SPECT images. (b) A series of concentric rings (R_0, R_1,..., R_{n-1}), the outer ring denoted R_0, and the inner ring denoted R_{n-1}. Each ring is divided into 40 sectors.

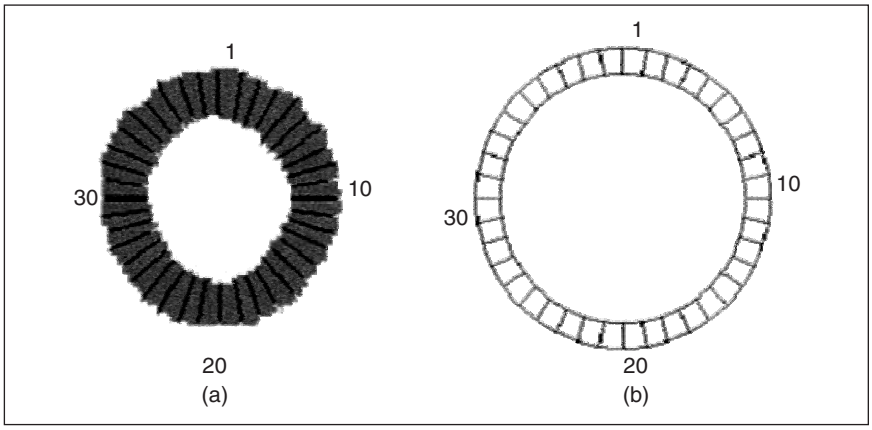

7. Relationship between cerebral cortical regions in a HMPAO brain slice and a concentric ring in a bullseye plot. (a) Cerebral cortical region. (b) Its corresponding ring.

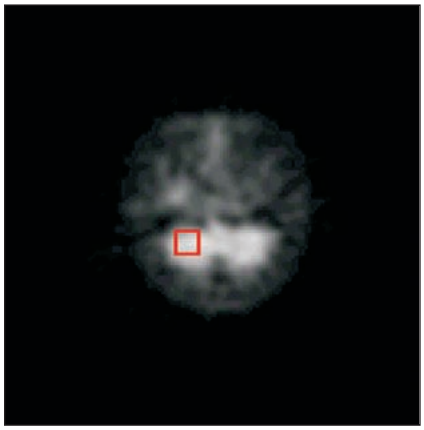

8. Rectangular region in the cerebellum region is selected as the reference region.

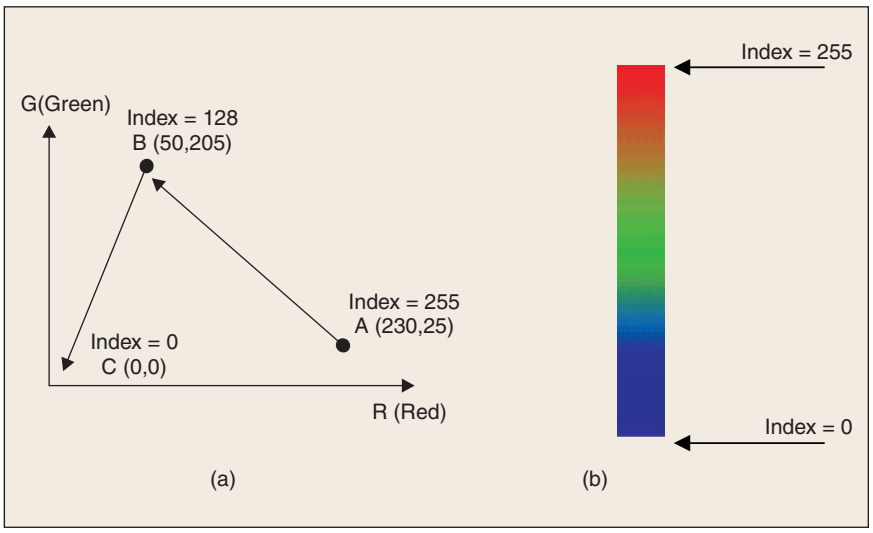

9. (a) Schema to obtain the corresponding RGB (*R*+*G*+*B*=255) value of each color index. (b) Color index and its color palette.

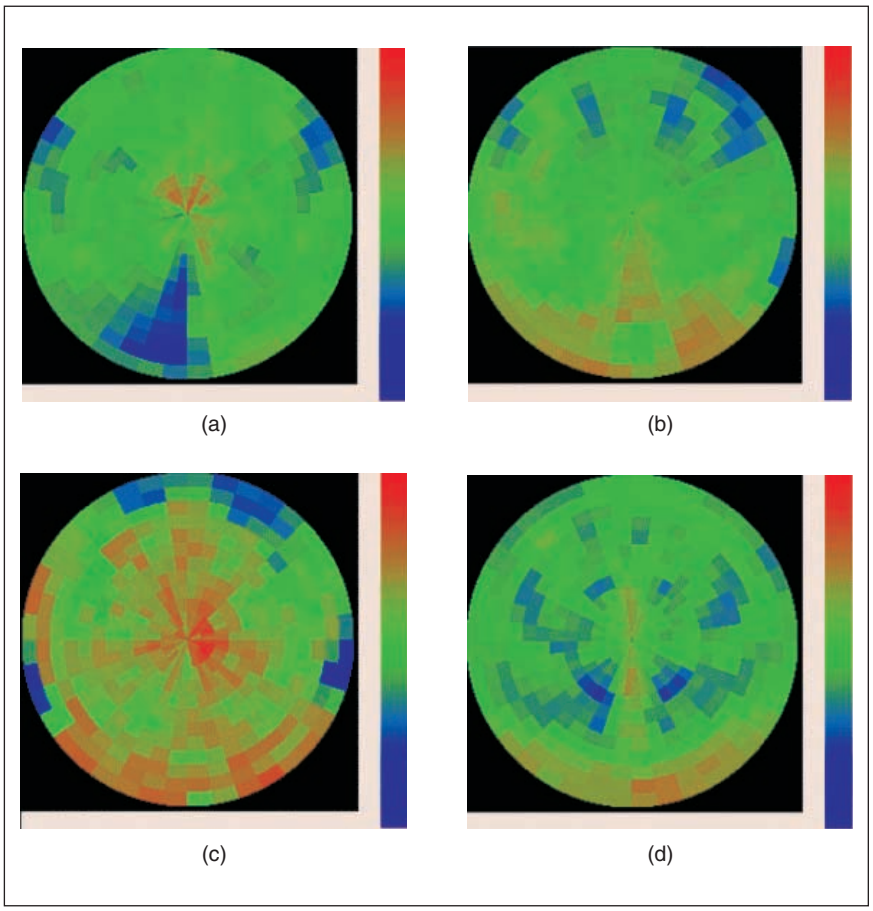

10. (a) Bullseye shows an area of markedly decreased cerebral perfusion in the right occipital area due to occlusion of right posterior cerebral artery. (b) Bullseye in a case with chronic motor and vocal tics shows decreased cerebral perfusion in bilateral frontal areas. (c) In a patient with frontal-lobe dementia, decreased perfusion in the bilateral frontal lobes is demonstrated by bullseye. (d) Characteristic pattern of decreased cerebral blood flow in bilateral posterior parietal and temporal lobes in a case of Alzheimer's dementia.

desirable for physicians in the diagnoses of various brain diseases.

Acknowledgments

This work was supported by the National Council of Nuclear Energy, Taiwan, under grants NSC 87-2218-E006 and NSC 89-NU-7-006-001.

Yung-Nien Sun received his B.S. degree from National Chiao Tung University, Hsin-Chu, Taiwan, Republic of China, in 1978 and the M.S. and Ph.D. degrees from University of Pittsburgh, Pittsburgh, Pennsylvania, in 1983 and 1987, respectively. He was an assistant scientist with the Brookhaven National Laboratory, New York, from 1987 to 1989. He joined the National Cheng Kung University, Taiwan, in 1989 as associate professor and was the chairman of the department from 1996 until 1999. He is currently a professor there in the Department of Computer Science and Information Engineering. His research interests are in medical image analysis, computer graphics, and vision. He is a member of IEEE, Sigma-Xi, the Chinese Association of Image Processing and Pattern Recognition, and the Chinese Association of Biomedical Engineering.

Shu-Chien Huang was born in Pingtung, Taiwan, in 1968. He received his B.S. in computer information education from National Taiwan Normal University in 1992. He received his M.S. and Ph.D. in computer science and information engineering from National Cheng Kung University in 1994 and 1999, respectively. He is currently an assistant professor in the Department of Computer Science, National Pingtung Teachers College, Taiwan. His research focuses on image processing, pattern recognition, and computer graphics.

Nan-Tsing Chiu received his M.D. degree from the College of Medicine, Kaohsiung Medical University, Taiwan, in 1987 and his M.S. degree in biomedical engineering from National Cheng Kung University, Taiwan, in 1992. He is currently an associate professor at the Department of Nuclear Medicine, National Cheng Kung University Medical College, and director of the Nuclear Medicine Department at the University Medical Center. His research interests include nuclear medicine diagnosis, radioisotope therapy, and computer-assisted diagnosis.

Chin-Yin Yu received her M.B. degree from the School of Medicine, National Taiwan University, Taiwan, in 1980. She received a two-year fellowship in MRI and neuroradiology at UCLA and UCSF in 1985-1987 and had another, six-month fellowship in cardiac MRI at Washington University at St. Louis in 1993. She is currently the director of neuroradiology at the Medical Center of National Cheng Kung University. Her research interests include blood flow dynamics of the brain and heart, brain perfusion, MRS of brain metabolites, and fMRI of the brain.

Fwu-Jeng Chen received his B.S. degree in information engineering from Chung Yuan University, Chung Li, Taiwan, in 1996 and his M.S. degree in computer science and information engineering from National Cheng Kung University, Tainan, in 1998. He is currently with R&D Division, VIA Technologies, Inc., Hsin Chu, Taiwan. His research interests include image processing, neural networks, graph theory, and algorithms.

Address for Correspondence: Yung-Nien Sun, Department of Computer Science and Information Engineering, National Cheng Kung University, Tainan, Taiwan. E-mail :ynsun@mail.ncku.edu.tw. Fax: 886 6 2747076. Tel: +886 6 2757575, ext. 62526.

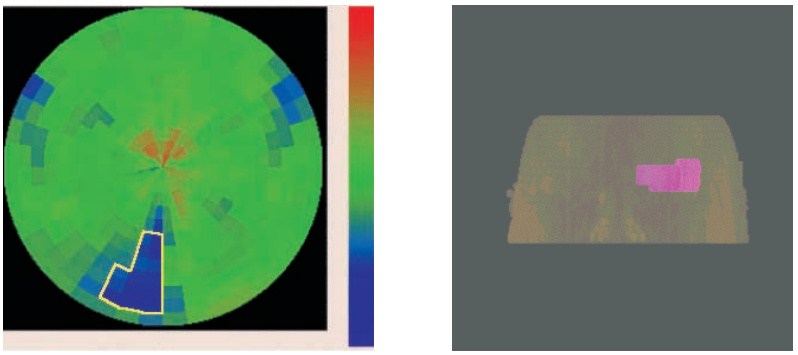

11. Geometrical relationship between defect in the 3-D head model and in the bulls-eye plot of Figure 10(a). (a) Diseased sectors surrounded by the yellow polygon and reflecting low radioactivity. (b)-(d) 3-D visualization of the defect and head model simultaneously from three different views by the semi-boundary display method.

References

[1] R.A. Holmes, S.B. Chaplin, K.G. Royston, T.J. Hoffman, W.A. Volkert, D.P. Nowotnik, L.R. Canning, S.A. Cumming, R.C. Harrison, and B. Higley, "Cerebral uptake and retention of 99m Tc-hexamethyl-propyleneamine oxime," *Nucl. Med. Commun.*, vol. 6, pp. 443-447, 1985.

[2] B.L. Holman and M.D. Devous, "Functional brain SPECT: The emergence of a powerful clinical method," *J. Nucl. Med.*, vol. 33, pp. 1888-1904, 1992.

[3] I. Podreka, E. Suess, G. Goldenberg, M. Steiner, T. Brucke, C. Muller, W. Lang, R.D. Neirinckx, and L. Deecke, "Initial experience with technetium-99m HMPAO brain SPECT," *J. Nucl. Med.*, vol. 15, pp. 9-15, 1989.

[4] J.L. Moretti, G. Defer, L. Cinotti, et al., "Luxury-perfusion with Tc-99m-HMPAO and I-123-IMP SPECT imaging during the subacute phase of stroke," *Eur. J. Nucl. Med.*, vol. 16, pp. 17-22, 1990.

[5] F. Grunwald, S. Zierz, K. Broich, S. Schumacher, A. Bockisch, and H.J. Biersack, "HMPAO-SPECT imaging resembling alzheimer-type dementia in mitochondrial encephalomyopathy with lactic acidosis and stroke-like episodes (MELAS)," *J. Nucl. Med.*, vol. 31, pp. 1740-1742, 1990.

[6] J.M. Mountz, L.C. Tolbert, D.W. Lill, C.R. Katholi, and H.G. Liu, "Functional deficits in autistic disorder: Characterization by Tc-99m-HMPAO and SPECT," *J. Nucl. Med.*, vol. 36, pp. 1156-1162, 1995.

[7] C.R. Rowe, F.B. Samuel, S.F. Berkovic, M.C. Austin, M. Saling, R.M. Kalnins, W.J. McKay, and P.F. Bladin, "Visual and quantitative analysis of interictal SPECT with Tc-99m-HMPAO in temporal lobe epilepsy," *J. Nucl. Med.*, vol. 32, pp. 1688-1694, 1991.

[8] J.H. Caldwell, D.L. Williams, G.D. Harp, J.R. Stratton, and J.L. Ritchie, "Quantitation of size of relative myocardial perfusion defect by single-photon emission computed tomography," *Circulation*, vol. 70, pp. 1048-1056, 1984.

[9] R. Eisner, A. Churchwell, T. Noever, D. Nowak, K. Cloninger, D. Dunn, W. Carlson, J. Oates, J. Jones, and D. Morris, "Quantitative analysis of the tomographic thallium-201 myocardial bullseye display: Critical role of correcting for patient motion," *J. Nucl. Med.*, vol. 29, pp. 91-98, 1988.

[10] R.L. Eisner, M.J. Tamas, K. Cloninger, D. Shonkoff, J.A. Oates, A.M. Gober, D.W. Dunn, J.A. Malko, A.L. Churchwell, and R.E. Patterson, "Normal SPECT thallium-201 bulls-eye display: Gender differences," *J. Nucl. Med.*, vol. 29, pp. 1901-1909, 1988.

[11] A.J. Da Silva, H.R. Tang, K.H. Wong, M.C. Wu, M.W. Dae, and B.H. Hasegawa, "Absolute in vivo quantitation of myocardial activity," *IEEE Trans. Nucl. Sci.*, vol. 47, no. 3, pp. 1093-1098, 2000.

[12] M.P. Sandler, J.A. Patton, R.E. Coleman, et al., *Diagnostic Nuclear Medicine*, 3rd ed. Baltimore, MD: Williams & Wilkins, 1996.

[13] R.M. Haralick, S.R. Sternberg, and X. Zhuang, "Image analysis using mathematical morphology," *IEEE Trans. Pattern Anal. Machine Intell.*, vol. PAMI-9, pp. 532-548, 1987.

[14] J.W. Klingler, C.L. Vaughan, T.D. Fraker, et al., "Segmentation of echocardiographic images using mathematical morphology," *IEEE Trans. Biomed. Eng.*, vol. 35, pp. 925-934, 1988.

[15] G. Borgefors, "Distance transformations in arbitrary dimensions," *Comput. Vis. Graph. Image Process.*, vol. 27, pp. 321-345, 1984.

[16] P.E. Danielsson, "Euclidean distance mapping," *Comput. Vis. Graph. Image Process.*, vol. 14, pp. 227-248, 1980.

[17] T. Saito and J.J. Toriwaki, "New algorithm for Euclidean distance transformation of an *n*-dimensional digitized picture with application," *Pattern Recognit.*, vol. 27, pp. 1551-1565, 1994.

[18] Y.N. Sun, S.C. Huang, T.C. Chang, et al., "Fast registration technique of MR and SPECT brain images," *Proc. SPIE*, vol. 3338, pp. 1442-1449, 1998.

[19] J.K. Udupa and D. Odhner, "Fast visualization, manipulation, and analysis of binary volumetric objects," *IEEE Trans. Graphics Applicat.*, vol. 11, no. 6, pp. 53-62, 1991.